Peak precipitation intensity in relation to atmospheric conditions and large-scale forcing at midlatitudes

Loriaux, Jessica M.; Lenderink, G.; Siebesma, A. Pier

DOI
10.1002/2015JD024274

Publication date
2016

Document Version
Final published version

Published in
Journal Of Geophysical Research-Atmospheres

AGU PUBLICATIONS

JGR

Journal of Geophysical Research: Atmospheres

RESEARCH ARTICLE
10.1002/2015JD024274

Key Points:
- Climatological analysis of relations between atmospheric conditions and precipitation extremes
- Heavy precipitation events occur under warmer, moister conditions, under stronger LS convergence
- Four atmospheric parameters were evaluated as precipitation indicators, but correlations were weak

Correspondence to:
J. M. Loriaux,
jmloriaux@gmail.com

Citation:
Loriaux, J. M., G. Lenderink, and A. Pier Siebesma (2016), Peak precipitation intensity in relation to atmospheric conditions and large-scale forcing at midlatitudes, *J. Geophys. Res. Atmos.*, *121*, 5471–5487, doi:10.1002/2015JD024274.

Received 25 SEP 2015
Accepted 27 APR 2016
Accepted article online 3 MAY 2016
Published online 25 MAY 2016

Peak precipitation intensity in relation to atmospheric conditions and large-scale forcing at midlatitudes

Jessica M. Loriaux[1,2], Geert Lenderink[1], and A. Pier Siebesma[1,2]

[1]Royal Netherlands Meteorological Institute, De Bilt, Netherlands, [2]Department of Civil Engineering, Delft University of Technology, Delft, Netherlands

Abstract Research on relations between atmospheric conditions and extreme precipitation is important to understand and model present-day climate extremes and assess how precipitation extremes might evolve in a future climate. Here we present a statistical analysis of the relation between large-scale conditions and hourly precipitation at midlatitudes, by using observations of the Netherlands combined with a regional reanalysis. The aim is to gain a better understanding of the typical large-scale atmospheric conditions and large-scale forcing associated with extreme hourly precipitation and determine the typical differences between cases of extreme precipitation and weaker events. To avoid double counting, we perform an event-based analysis and consider the hourly peak intensity, rather than all hourly data. Atmospheric large-scale profiles consistently show a clear separation between precipitation deciles, characterized by increasing instability and moisture content of the atmosphere for more extreme precipitation. Furthermore, stronger events are characterized by larger atmospheric forcing preceding the event, which primarily relates to vertical motions. Based on these results, four atmospheric parameters, describing atmospheric moisture, stability and large-scale convergence, are analyzed as potential indicators of strong precipitation events. Despite positive relations between these parameters and the peak intensity, their correlations are found to be weak.

1. Introduction

Due to the high-impact of extreme precipitation events on society, numerous studies have been done to assess the response of extreme precipitation to climate change [*Westra et al.*, 2014; *O'Gorman*, 2015]. There is general consensus that climate change will lead to a global increase in frequency and magnitude of extreme precipitation [*IPCC*, 2014] and observed changes are already being attributed to observed warming [*Min et al.*, 2011; *Pall et al.*, 2011; *Lenderink and Attema*, 2015].

Various studies describe the atmospheric conditions related to extreme precipitation events at midlatitudes by presenting detailed descriptions of mesoscale dynamics [*Houze*, 2004] or by describing essential ingredients for extreme events to occur [*Doswell et al.*, 1996]. These approaches are valuable, especially in the area of weather prediction, where detailed structures of the atmosphere at the mesoscale need to be considered for accurate forecasting. However, these studies are often based on analysis of a limited number of events or rather short periods [*Hand et al.*, 2004; *Ducrocq et al.*, 2013] and usually contain qualitative rather than quantitative descriptions. This limits the applicability for research in climate and climate change.

In view of climate and climate change, an important line of research focuses on the sensitivity of precipitation intensity to temperature and moisture. Observational studies of hourly precipitation over midlatitudes show sensitivities from 7% up to 14%/K for local precipitation extremes for a large range of temperatures [*Lenderink and Meijgaard*, 2008; *Lenderink and van Meijgaard*, 2010; *Berg et al.*, 2013; *Blenkinsop et al.*, 2015]. Whether these observed sensitivities can be used as guide for future changes remains an open question [*Westra et al.*, 2014]. They do not necessarily express a direct cause and effect relation, with precipitation responding to the higher moisture content of a warmer atmosphere. Furthermore, *Loriaux et al.* [2013] demonstrated that changes in atmospheric stability potentially affect the sensitivity results. Thus, observed sensitivities are likely connected to changes in circulation and atmospheric stability. Changes in atmospheric flow conditions are also likely to affect the changes in precipitation extremes in the future climate [*O'Gorman and Schneider*, 2009; *Emori and Brown*, 2005].

At midlatitudes, strong convection tends to occur ahead of synoptic disturbances, where upward vertical motions lead to moistening and destabilization of the atmosphere [*Doswell and Bosart*, 2001]. Studies have tried to connect extreme precipitation to cyclones [*Pfahl and Wernli*, 2012] and fronts [*Catto and Pfahl*, 2013]. A large amount of 6-hourly precipitation extremes were associated with fronts. Since many precipitation extremes occur under a combination of convective and large-scale precipitation, in this study we will not make an explicit distinction between the different precipitation types.

In order to determine what causes extremes, several studies have focused on the role of convective available potential energy (CAPE) and moisture. For example, *Lepore et al.* [2015] have analyzed the dependence of CAPE and dew point temperature for extreme precipitation in a climatological study over the U.S., finding that both parameters are of similar importance. The relations between tropical precipitation and large-scale moisture convergence and atmospheric stability parameters have been studied by *Davies et al.* [2013]. They found a strong relation between precipitation and moisture convergence, but no strong relation between atmospheric stability, such as measured by CAPE, and precipitation intensity. Another tropical study [*Dorrestijn et al.*, 2014] found a strong cross correlation between large-scale vertical velocity and deep convection.

A study for Europe showed weak correlations of extreme precipitation with CAPE, and stronger correlations with atmospheric moisture [*Barkidija and Fuchs*, 2013] based on radiosonde soundings, taken from nearby stations. The use of proximity data from radiosonde soundings or relatively low resolution global reanalysis data is widespread in studies relating extreme events to atmospheric conditions [*Dyson et al.*, 2014; *Craven and Brooks*, 2004; *Allen and Karoly*, 2014]. However, due to the coarse spatial resolution, these data may not always represent the atmospheric conditions very well.

With this study we aim to catalog the atmospheric conditions and large-scale forcing that accompany precipitation events of increasing intensities in a statistical sense. We will investigate how large-scale advection of moisture influences precipitation intensity and how these terms evolve over time. The atmospheric conditions are derived from a regional reanalysis using a downscaling of ERA-Interim, which provides high-resolution data both in time and space. These data are combined with surface observations, for instance, when deriving CAPE. Based on the combination of surface observations and model output, we furthermore evaluate several controlling factors for extreme precipitation. To this end, we investigate whether the large-scale vertical velocity and stability parameters correlate well over the Netherlands, since *Davies et al.* [2013] and *Dorrestijn et al.* [2014] show a strong correlation between tropical precipitation and vertical velocity but weak correlations for stability parameters. Furthermore, the water vapor path is evaluated as a potential indicator for extreme events, as this is also an often used sensitivity parameter for tropical precipitation [*Bretherton and Peters*, 2004; *Peters and Neelin*, 2006].

To summarize, we aim to realize a better understanding of atmospheric conditions for the precipitating atmosphere at midlatitudes and assess potential indicators for extreme precipitation events at midlatitudes. To this end, we first present the data sets used and the postprocessing of the data in section 2. Section 3 contains an analysis of the atmospheric profiles and large-scale forcing and their temporal evolution. This is followed by a comprehensive survey of potential precipitation indicators in section 4. To conclude, in section 5 we present a summary of our findings.

2. Data and Methods

In this study, we try to identify typical midlatitudinal atmospheric conditions for precipitation events and examine the relations between these conditions and precipitation intensity, with an emphasis on the more extreme precipitation events. To this end, we first analyze the environmental profiles of moisture, temperature, and large-scale forcing, followed by an analysis of several potential indicators of extreme precipitation, based on moisture, stability, and convergence. This analysis uses in situ precipitation observations and constrained model results, which are evaluated in an event-based setting.

The precipitation data set consists of the Royal Netherlands Meteorological Institute hourly rain gauge data from 1995 to 28 June 2014 [*KNMI*, 2014]. Measurements from 34 automated weather stations (AWSs) across the Netherlands are used (Figure 1), resulting in 5.8 million hours of data, of which $2.4 \cdot 10^5$ h (i.e., 4%) are wet (> 0.5 mm/h).

The atmospheric profiles and other large-scale atmospheric conditions are determined for the same period, using the high-resolution Regional Atmospheric Climate Model (RACMO) [*Van Meijgaard et al.*, 2008]. RACMO

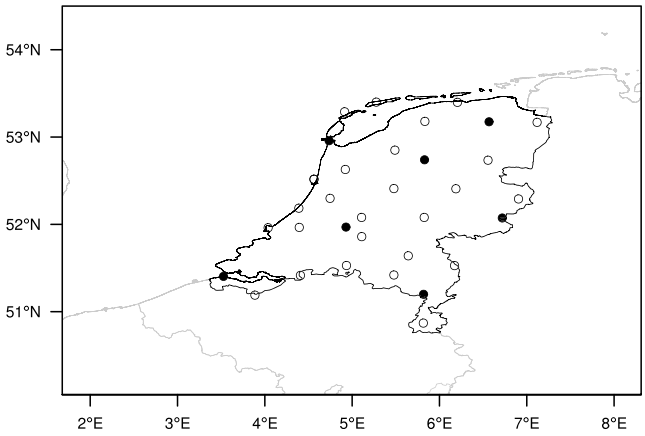

Figure 1. Map of the locations of the in situ observations (open and closed circles). The RACMO point data are available at the same locations. The closed circles are locations for which RACMO profile data are available, which will be used in section 3. The area of this figure is the area used to calculate large-scale vertical velocity, ω_{LS}.

has been used as an interpolator of the ERA-Interim reanalysis [*Dee et al.*, 2011] by performing short 36 h forecasts starting from 12 UTC. These forecasts are initialized from ERA-Interim and use ERA-Interim boundary fields. The model forecasts from 12 h to 36 h are used to build a continuous data set of atmospheric conditions. While the atmospheric profiles are comparable with ERA-Interim, the RACMO output is available at a high resolution (12 km and (sub)hourly), making it more suitable for this purpose. Model output consists of surface data that have been interpolated to all 34 AWS station locations, profile data that have been interpolated to 7 AWS stations spread out across the Netherlands (closed circles in Figure 1), and several cross sections of the vertical velocity. An overview of the data that have been used can be found in Table 1.

In section 3, we analyze large-scale potential temperature, specific and relative humidity, and vertical velocity profiles as well as the temperature and moisture tendency profiles, by combining hourly mean profiles based on 4 min snapshots from the seven locations marked by closed circles in Figure 1, into one large-scale profile over the Netherlands. Furthermore, in section 4 we study several atmospheric parameters that might be relevant as precipitation indicators: the large-scale vertical velocity at 700 hPa (ω_{LS}), convective available potential energy (CAPE), the water vapor path (WVP), and the *K* index. These hourly parameters are obtained from the RACMO output in different ways.

The vertical velocity is a highly fluctuating parameter. In order to get a good estimation of the large-scale vertical velocity, we therefore make use of a cross section of the vertical velocity at 700 hPa. This is done by taking a field average of the hourly instantaneous vertical velocity over an area of approximately 50.05°N–54.5°N by 1.68°E–8.31°E. This corresponds to the area displayed in Figure 1 (approximately 450 km × 500 km). Smaller areas were also used, but this did not affect the data (not shown). The obtained hourly ω_{LS} is used at all 34 locations corresponding to the AWS stations shown in Figure 1. Unfortunately, this method cannot be extended to the profiles of the vertical velocity, since we only have three cross sections. Therefore, the vertical velocity profile used in section 3 has been determined by combining the profiles of the seven station locations instead.

The hourly mean water vapor path based on 4 min snapshots is available at all 34 locations. At the same locations, hourly snapshot profiles of temperature and specific humidity are used to calculate the *K* index and CAPE.

The *K* index is originally an indicator for the likelihood of thunderstorms to occur [*Charba*, 1977]. It uses the temperature lapse rate (LTS, first right-hand side (RHS) term), lower atmospheric moisture content (LLM,

Table 1. Overview of the Data Used[a]

Source	Variable	Spatial Resolution	Postprocessed
AWS	precipitation intensity	34 stations	34 stations
	surface T, q_v	34 stations	34 stations
RACMO	ω_{LS} (700 hPa)	12 km × 12 km	area mean
	profiles (T, q_v, RH, ω)	7 stations	mean profile
	surface (WVP, T, q_v)	34 stations	34 stations

[a]The locations of the stations can be found in Figure 1, along with the domain over which the large-scale vertical velocity was calculated.

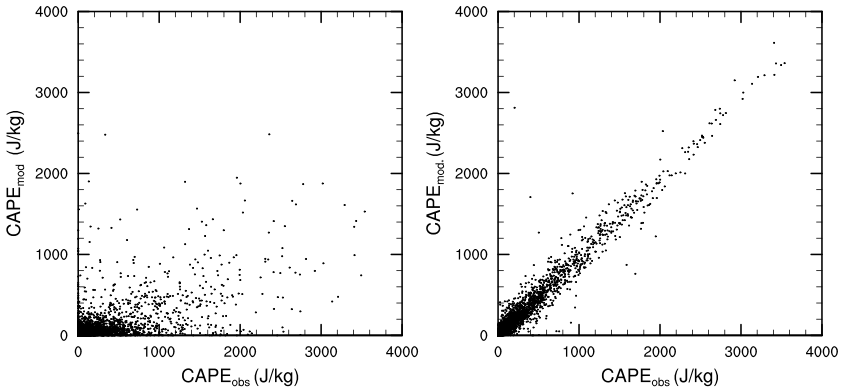

Figure 2. Scatterplot of (left) CAPE from soundings versus CAPE calculated for RACMO data and (right) CAPE supplemented with surface temperature and specific humidity from the sounding data.

second RHS term), and midlevel relative humidity (MLH, third RHS term) of the atmosphere:

$$K_{\mathrm{IDX}} = (T_{850\mathrm{hPa}} - T_{500\mathrm{hPa}}) + T_{d,850\mathrm{hPa}} - (T_{700\mathrm{hPa}} - T_{d,700\mathrm{hPa}}). \quad (1)$$

An alternative method for calculating the *K* index was presented by *Davies et al.* [2013]. The alternative *K* index uses a mean of (dew point) temperature values at 1000 hPa and 850 hPa, rather than 850 hPa. Both *K* indexes have been analyzed and lead to similar results. Since it is more widely used, in this document we will present results for the established *K* index.

CAPE is calculated from hourly RACMO temperature and specific humidity profiles at all station locations in Figure 1, using

$$\mathrm{CAPE} = \int_{z_0}^{z_t} g \frac{T_{v,p} - T_{v,e}}{T_{v,e}} \mathrm{d}z, \quad (2)$$

which describes the vertical integral of the buoyancy, calculated from the difference between the virtual temperature of the parcel, $T_{v,p}$, and the environment, $T_{v,e}$, along with the gravitational constant, g. Here the lower bound of the integral, z_0, is the level of free convection, while the upper bound of the integral, z_t, is the height of the equilibrium level, so that CAPE is calculated over the region above cloud base, where the temperature excess is positive. The parcel is released near the surface.

Figure 2 shows scatterplots for CAPE calculated from radiosonde data at 12 UTC at station De Bilt (KNMI) against CAPE calculated from the modeled temperature, humidity, and pressure profiles from RACMO over the period 1995 to 2012 (left). The modeled CAPE underestimates the CAPE based on radiosonde data. Profile analysis (not shown) suggests that this is primarily due to the underestimation by the model of near-surface high moisture conditions that sometimes accompany high CAPE values. To overcome this, we calculated CAPE for RACMO profiles where the parcel profiles were initialized with 2 m specific humidity and temperature from the radiosonde (Figure 2, right). It is clear that this greatly improves the results. Apparently, the RACMO profiles beyond the surface layer are very accurate. In this study, we have therefore enhanced the CAPE calculations using RACMO profiles, by initializing the parcel profiles with 2 m specific humidity and temperature from the KNMI in situ data set. These data are available at the same temporal resolution and station locations as the precipitation observations.

In order to avoid double counting and scatter in the analysis of the relation between atmospheric conditions and the precipitation strength, we will analyze the data in terms of precipitation events. The strength of the event will be measured by its peak intensity, i.e., the highest measured hourly precipitation intensity during the event. Previous studies [*Gaál et al.*, 2014; *Molnar et al.*, 2015] have proposed a way to organize rain gauge data into events by using a precipitation threshold and a dry interval to separate events. We have applied a similar method. However, the stations used are often located close together. Since one event can pass multiple stations, we have also added a spatial condition. This way, events that are spaced too closely together are also connected.

This means that precipitation events are formed based on a precipitation threshold, a minimum dry interval (separation time), and a minimum distance between events (spatial threshold). We use a precipitation

Table 2. Peak Intensities (mm/h) and Their Range for Each Decile Bin[a]

Deciles	Decile Range	Peak Intensity	Intensity Range
10%	0%–10%	0.51	0.5–0.6
20%	10%–20%	0.64	0.6–0.7
30%	20%–30%	0.79	0.7–0.9
40%	30%–40%	0.99	0.9–1.1
50%	40%–50%	1.24	1.1–1.4
60%	50%–60%	1.56	1.4–1.8
70%	60%–70%	1.99	1.8–2.3
80%	70%–80%	2.62	2.3–3.0
90%	80%–90%	3.74	3.0–4.7
100%	90%–100%	8.40	4.7–79
Percentiles	Percentile Range	Peak Intensity	Intensity Range
91%	90%–91%	4.83	4.7–5.0
92%	91%–92%	5.13	5.0–5.3
93%	92%–93%	5.49	5.3–5.7
94%	93%–94%	5.91	5.7–6.1
95%	94%–95%	6.43	6.1–6.7
96%	95%–96%	7.12	6.7–7.6
97%	96%–97%	8.07	7.6–8.7
98%	97%–98%	9.43	8.7–10.3
99%	98%–99%	11.67	10.3–13.7
100%	99%–100%	19.98	13.7–79

[a]There are 4447 data points in each bin. The percentile bins (444 points per bin) are shown below the horizontal line.

threshold of 0.5 mm/h, considering all other data as dry. Following *Gaál et al.* [2014] and *Molnar et al.* [2015], a separation time of 2 h is used. The spatial threshold has been set at 50 km. Increasing this parameter reduces the amount of scatter and also causes a reduction in the amount of events, while decreasing the spatial threshold leads to an increase of scatter as well as events. Overall, the results are not greatly affected by adjusting this parameter.

Using a precipitation threshold of 0.5 mm/h, separation time of 2 h, and distance of 50 km, we are left with 44,475 separate precipitation events. For each event, we have determined the peak precipitation intensity. The atmospheric data are selected for the corresponding time $\pm$12 h and (if applicable) location of the peak intensity.

This is a coarse but effective method to ensure that extreme intensities belonging to the same event are not double counted. However, sometimes unrelated events can also be connected, and only the highest intensity of this selection will be used in our analysis. As a result, weaker peak intensities are a bit underrepresented in the statistics, and event characteristics such as the duration are not reliable.

For part of our analysis, the event data are grouped into bins separated by deciles of the peak intensity of the event, so that changes in behavior from mild to heavy precipitation events can be seen. Table 2 shows the decile bins, along with the mean peak intensity and the intensity range within the bin. In section 4, we will look at potential indicators, and it will be useful to zoom in on more extreme events. Therefore, the highest decile has also been split up into percentile bins. With a mean peak intensity of nearly 20 mm/h, the top percentile bin contains the strongest precipitation events.

3. Atmospheric Forcing and Response

We start our examination of the precipitating atmosphere by analyzing the atmospheric conditions and large-scale tendency profiles. Figure 3 shows the mean atmospheric profiles of relevant parameters for deciles of the peak precipitation intensity. These profiles are taken 3 h prior to the peak intensity of the event, to minimize event-induced effects. They are created by combining hourly profiles from seven station locations in the

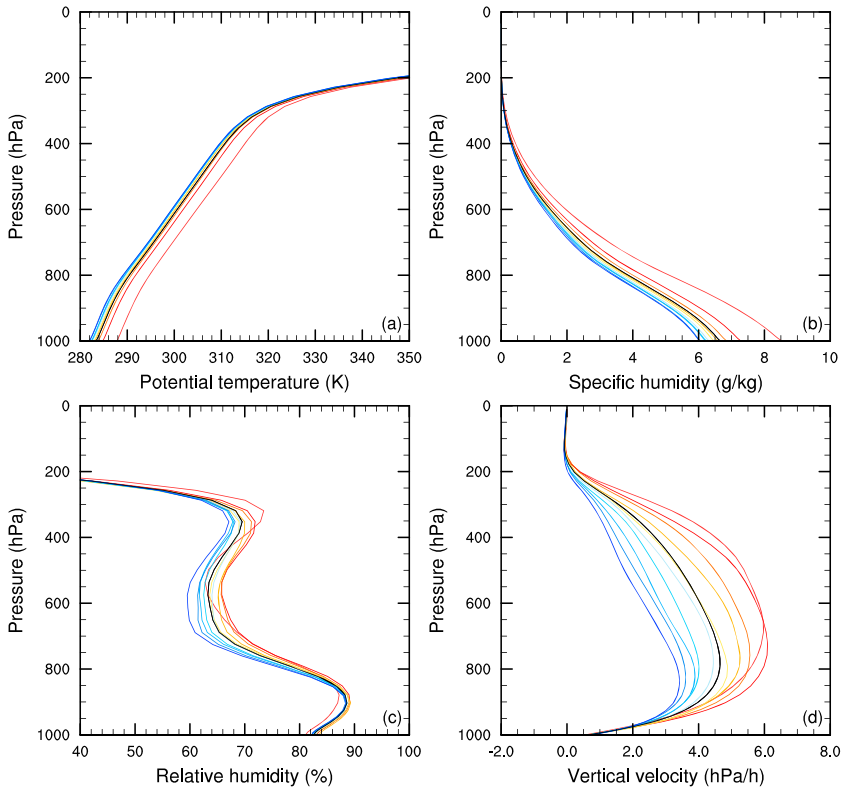

Figure 3. Atmospheric profiles of (a) potential temperature, (b) specific humidity, (c) relative humidity, and (d) vertical velocity, 3 h prior to the peak precipitation intensity of the event. The mean profile is shown in black, while the profiles for precipitation deciles are shown from blue (weak precipitation) to red (strong precipitation).

Netherlands (closed circles in Figure 1), by means of a spatial average over these seven stations. The profiles are depicted for precipitation bins, separated by the precipitation deciles (Table 2), and increase in strength from blue to red.

Figure 3a shows the hourly mean potential temperature profile of the environment. The tropopause is located at around 250 hPa. As expected, an increase in temperature at all levels is observed for increasing precipitation deciles. Figure 3b shows the specific humidity, q_v. While q_v increases over the full profile with increasing precipitation deciles, the absolute difference between deciles is largest near the surface. Both the temperature and moisture profiles show the most pronounced increase for the highest precipitation decile bin.

The temperature and moisture profiles are combined in Figure 3c, which shows the relative humidity profiles. Interestingly, while the first through ninth deciles show a steady increase of relative humidity with increasing peak intensity, the highest precipitation decile has a deviating profile. Both surface and midtropospheric relative humidity are lower than most of the weaker deciles. This shows that for the most extreme precipitation events, the temperature increase with respect to less extreme deciles dominates over the increase in specific humidity, leading to a lower relative humidity.

Figure 3d shows the vertical velocity (ω) which is an indirect measure of the large-scale convergence. Note that we have defined ω positive in the upward direction. All of the decile bins show upward motion, which increases until it peaks somewhere between 850 (weak precipitation) and 700 hPa (strong precipitation), after which the vertical velocity decreases again, approaching zero as the tropopause is reached. Note that the upper decile bin has a slightly different shape than the weaker deciles, which may be an indication of different large-scale dynamics.

Although the order of magnitude of the maximum vertical velocity is quite similar for strong precipitation, these profiles differ from more tropical vertical velocity profiles [*Davies et al.*, 2013]. For weaker precipitation we still find upward vertical velocity, while *Davies et al.* [2013] see downward motion over a large pressure range for most precipitation deciles in the tropics.

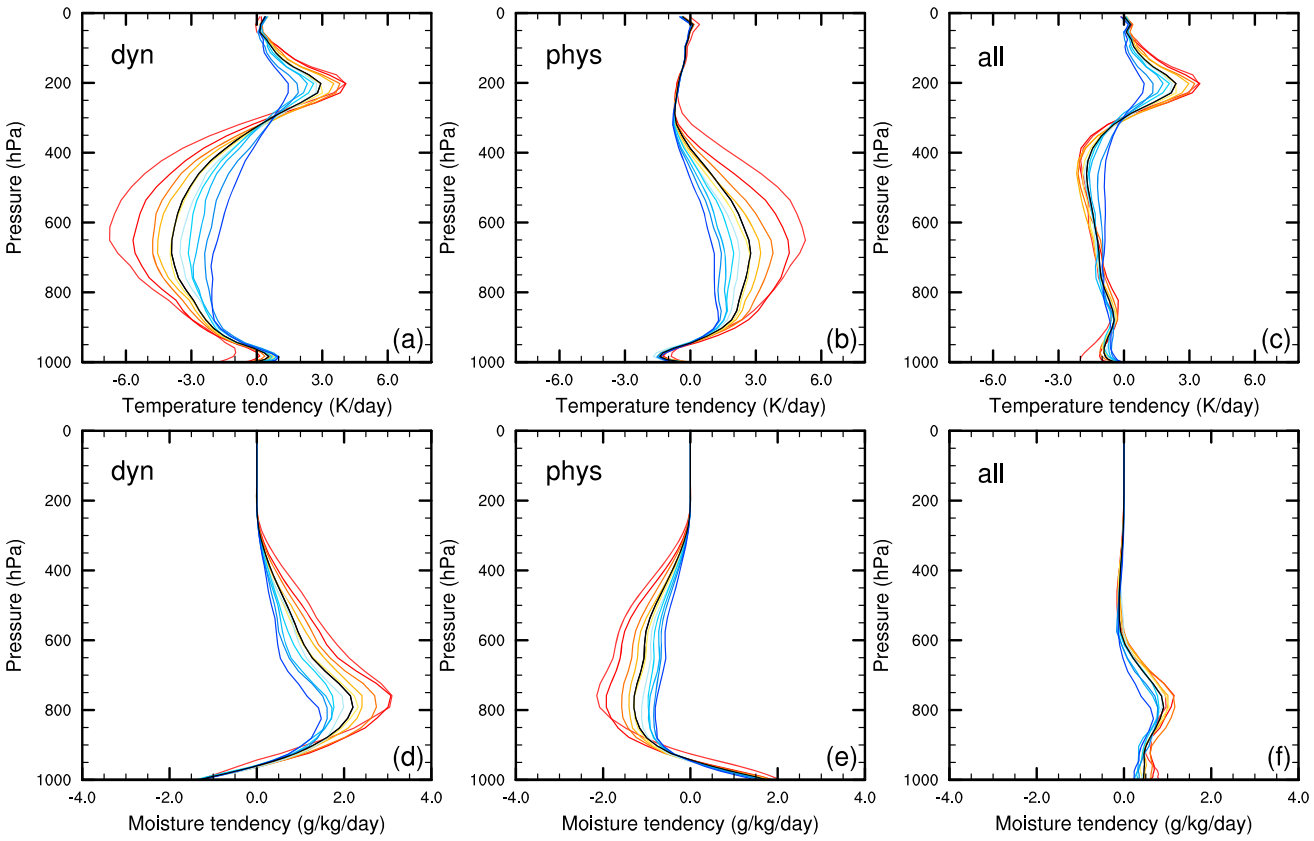

Figure 4. Atmospheric tendency profiles of (a–c) temperature and (d–f) specific humidity 3 h prior to the peak precipitation intensity of the event. The dynamical (Figures 4a and 4d) and physical (Figures 4b and 4e) contributions are followed by the total tendency profiles in Figures 4c and 4f. Colors are as described in Figure 3.

Next, we look at the 1 h mean temperature (a–c) and specific humidity tendencies (d–f) in Figure 4. Apart from the total tendencies, the model provides a decomposition into dynamical and physical components. The dynamical component gives the tendency contribution due to resolved processes, i.e., horizontal and vertical advection, while the physics component contains the tendencies caused by model parameterizations, such as the radiation, convection, and condensation. In Figure 4, the dynamical (a and d) and physical (b and e) components are shown separately, as well as the sum of both components (c and f).

The dynamical component of the temperature tendency shows cooling up to 400 to 300 hPa (weak, respectively strong precipitation), which destabilizes the temperature profile. This is mostly due to vertical advection (not shown), which means that the dynamical tendency is largely influenced by the vertical velocity profiles shown in Figure 3d. The dynamical temperature tendency is largest for the highest precipitation decile and peaks at −7 K/d, near 650 hPa. The lower deciles show the same pattern, but with lower values and peaking at lower altitudes. Above the cooling layer, the tendency is positive, peaking on average at 3 K d^{-1} around 200 hPa. This can be explained by the drop in tropopause height as the event approaches. As can be seen from the dynamical moisture tendency profile, the tropospheric cooling is accompanied by a moistening of the troposphere, apart from the boundary layer. Again, this is mainly caused by the vertical advection. Similar to the vertical velocity and dynamical temperature tendency profiles, the signal is strongest for the highest precipitation decile, showing a moistening of 3 g kg^{-1} d^{-1} at 750 hPa. This moistening and cooling of the layer leads to conditions more favorable for convection and condensation.

The physical tendency components show cooling and moistening near the surface, but drying and warming in the rest of the troposphere, indicating possible condensation and condensational heating as a result of the dynamical tendencies. Again, we see a clear stratification for the precipitation deciles, with the strongest tendencies (5 K d^{-1}, −2 g kg^{-1} d^{-1}) occurring for the highest precipitation deciles.

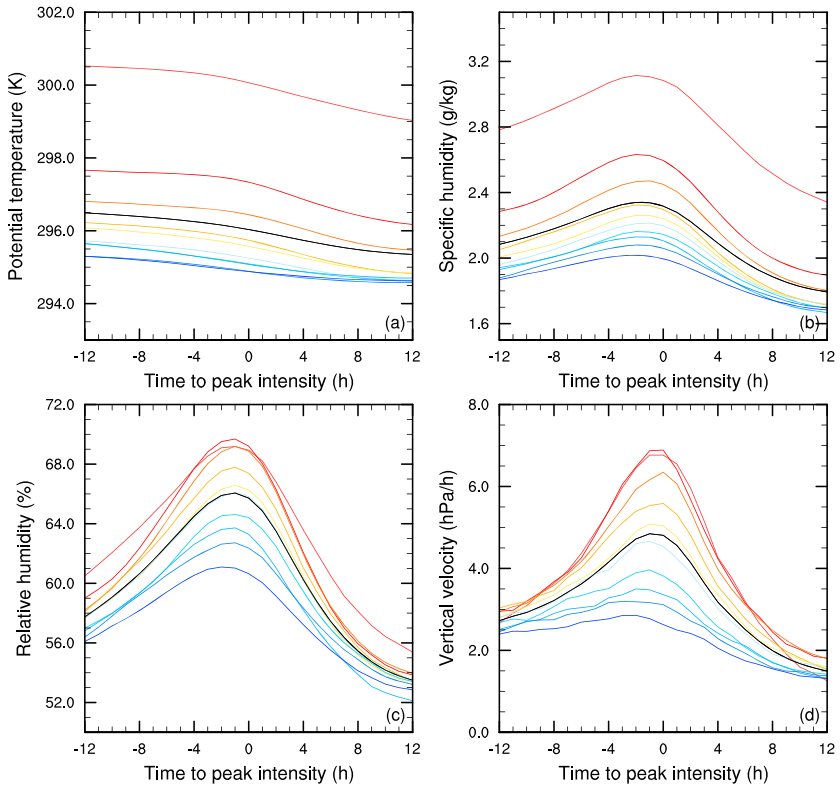

Figure 5. Temporal evolution of the atmospheric profiles of (a) potential temperature, (b) specific humidity, (c) relative humidity, and (d) vertical velocity at 700 hPa, from 12 h prior to 12 h after the time of the peak intensity of the event. Colors are as described in Figure 3.

The combined dynamical and physical temperature contributions show cooling from the surface up to approximately 300 hPa that is weak and near constant with height for the lowest deciles but becomes more stratified and increases to -2 K d^{-1} at 400 hPa for the highest deciles. There is quite a strong warming tendency above 300 hPa, peaking at 3.5 K d^{-1} since the dynamical contribution is not compensated by a strong physical cooling component. The combined moisture tendency shows moistening of the atmospheric profile up to approximately 600 hPa, which increases with increasing precipitation deciles. At higher levels, the physical and dynamical contributions approximately cancel each other out. For both moisture and temperature tendencies, the dynamical contribution appears to dominate over the physical contribution, and tendencies are stronger for the highest precipitation deciles. However, the combined moisture and temperature tendencies are both much weaker than the separate dynamical and physical components. Though the separation into dynamical and physical tendency components is not exactly the same as a separation into large-scale and convective tendency components, it is interesting to note the parallel with the work of *Zhang* [2002, 2003], suggesting that the atmosphere is close to convective quasi-equilibrium.

To get a better idea of the changing atmospheric state and the timing of separate tendency contributions, we also look at the temporal evolution of these terms. Since the vertical velocity and tendency profiles all peak between 650 and 750 hPa, we have chosen to analyze the temporal evolution of the profiles at 700 hPa (Figures 5 and 6).

Figure 5 shows the temporal evolution of the atmospheric profiles of Figure 3 from 12 h before to 12 h after the peak intensity. The potential temperature (Figure 5a) shows cooling of approximately 0.5 to 1.5 K/d for weak to strong precipitation deciles, respectively. During the full period, the temperature tends to be higher for the higher precipitation deciles. The temporal evolution of the specific humidity (Figure 5b) shows the strongest pre-event moistening for the highest precipitation deciles. For lower deciles the temporal signal is much weaker. After the peak intensity is reached, the specific humidity decreases to values below the initial specific humidity for each decile bin. Figure 5c shows the temporal evolution of the relative humidity. At 700 hPa, the highest precipitation decile does not yet show the decrease in relative humidity with respect

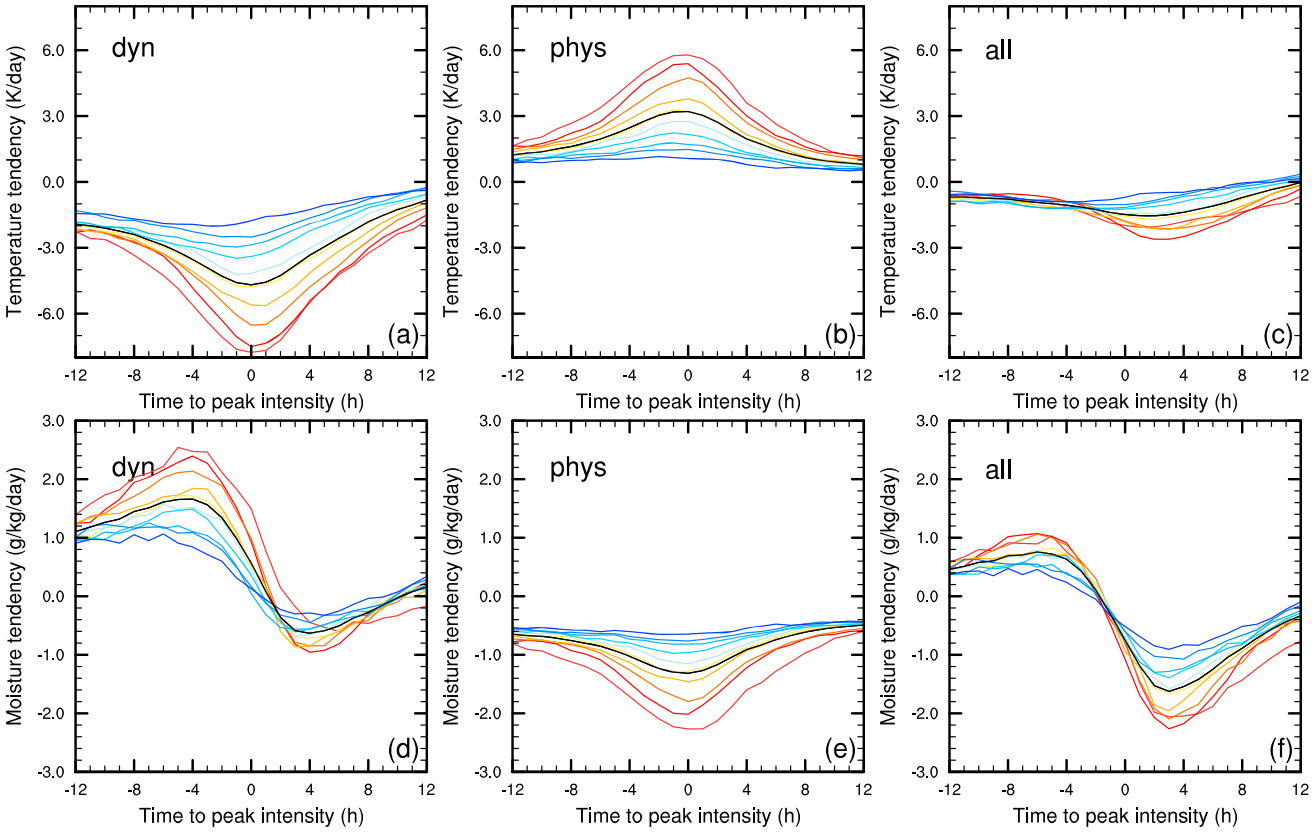

Figure 6. Temporal evolution of the (a–c) atmospheric temperature and (d–f) specific humidity tendencies at 700 hPa from 12 h prior to 12 h after the time of the peak intensity of the event. The dynamical (Figures 6a and 6d) and physical contributions (Figures 6b and 6e) are followed by the total tendency profiles in Figures 6c and 6f. Colors are as described in Figure 3.

to the lower precipitation deciles seen in Figure 3c. Therefore, the temporal evolution does not show a clear deviation between the highest decile and the other deciles. The relative humidity simply increases as the event approaches, after which the relative humidity decreases to below starting values. The vertical velocity (Figure 5d) has a strong stratification, with weak temporal variations for the lowest precipitation deciles, but a very clear increase leading up to the time of the peak intensity, after which the vertical velocity rapidly decreases to approximately 2 hPa/h, which is slightly lower than the starting value. To summarize, at 700 hPa, weak and strong precipitation events all lead to cooling of the layer, with moistening and an increase in vertical velocity leading up to the event, followed by drying and a decrease in large-scale vertical velocity. Eventually, the atmosphere is left in a colder, drier state, with weaker large-scale convergence. These effects are most pronounced in the highest deciles.

Next, we look at the temporal evolution of the temperature and moisture tendencies (Figure 6). The dynamical (Figure 6a) and physical (Figure 6b) temperature tendency components both show the strongest temporal signal for the highest precipitation deciles. Prior to the event, there is cooling due to vertical advection which increases as the event approaches (Figure 6a). Simultaneously, the physical component of the temperature tendency (Figure 6b) increases as well, indicating that convection and condensational heating are already taking place, compensating for the destabilizing cold air advection. There is no time lag between the physical and dynamical components, and the total temperature tendency is fairly constant and shows little stratification up to 3 h before the peak intensity of the event. After that, the highest precipitation deciles show a net cooling which increases up to approximately 3 h after the peak intensity and decreases until the temperature tendency almost vanishes. This is in line with our earlier observation that the system is close to quasi-equilibrium, even for the highest precipitation deciles.

The moisture tendencies (Figures 6d–6f) also show the strongest temporal signals for the highest precipitation deciles. The dynamical component (Figure 6d) clearly shows advection of moist air, which peaks 4 h before the height of the event. The physical component of the moisture tendency (Figure 6e) lags behind, peaking

at the time of the event. This time lag indicates that the moistening precedes the condensation, which unsurprisingly peaks at the time of the peak intensity. The combined effect (Figure 6f) is a moistening of the layer due to advection of moist air, which is followed by drying of the layer, due to the event itself.

4. Precipitation Indicators

The clear stratifications and temporal signals seen for the profiles discussed in section 3 indicate interaction between precipitation and vertical velocity, moisture, and stability. Therefore, we next look at a few relevant parameters and evaluate their potential role as indicators for extreme precipitation.

Over the tropics, the large-scale vertical velocity correlates well with deep convection [*Dorrestijn et al.*, 2014], and large-scale moisture convergence relates well with tropical total precipitation [*Davies et al.*, 2013]. We will therefore continue the analysis of the vertical velocity in this section to determine its potential as an indicator for heavy precipitation over midlatitudes. In the previous section, we already analyzed the vertical velocity profile and its temporal evolution at 700 hPa, based on seven locations, and observed a clear decile stratification of this parameter. As the vertical velocity is a highly fluctuating parameter, we will use the 700 hPa field mean vertical velocity, ω_{LS}, rather than the profile cross section used before.

A highly unstable atmosphere leads to vigorous convection, which can result in strong precipitation intensities. This can also be seen in the dynamical temperature tendency profile in Figure 4a, which shows the strongest destabilization of the atmosphere for the highest precipitation decile. Using an entraining plume model, *Loriaux et al.* [2013] have shown that the sensitivity of precipitation intensity to temperature increases with atmospheric instability. Here we investigate if the atmospheric stability itself is a good indicator of extreme precipitation by examining the relation between CAPE and peak precipitation intensity.

The systematic intensification of the moisture tendency profiles with increasing precipitation deciles confirms that there is also a relation between atmospheric moisture and the precipitation intensity. Furthermore, tropical precipitation intensities exhibit critical behavior in relation to the water vapor path [*Peters and Neelin*, 2006]. Therefore, we will also evaluate the water vapor path (WVP).

Lastly, we will consider the *K* index, a parameter which incorporates both stability and moisture, to determine if a combined effect leads to a better precipitation indicator. The *K* index is originally an indicator for the likelihood of thunderstorms to occur and is based on the temperature lapse rate and atmospheric moisture components, as was shown in equation (1). The highest *K* index values are reached when the atmosphere is moist and unstable with high low-level moisture. Therefore, we expect to find a positive relationship between the *K* index and precipitation intensity. An advantage of this parameter is that it is not affected by the surface conditions as much as CAPE is. Therefore, the *K* index is more robust in space and time.

We will first consider the temporal evolution of the parameters separated into groups based on precipitation intensity, as was done in section 3. Next we analyze the relation between the peak intensity and the atmospheric parameters directly. This will illustrate which precipitation intensity is most observed for a certain value of the atmospheric parameter, rather than separating the atmospheric parameter into precipitation deciles. Finally, a lag correlation analysis is done to determine how peak precipitation responds to the parameters and at what time the correlation is highest.

4.1. Average Temporal Evolution

Unsurprisingly, the temporal evolution of the large-scale vertical velocity (Figure 7a) compares well with our first approximation based on the vertical velocity profile (Figure 5d), albeit with slight differences. Note that the top decile has been split up into percentile bins (dashed) to emphasize the extreme intensities. The vertical velocity peaks a few hours before the maximum intensity of the event and drops to approximately 1 hPa/h for all percentiles, which is weaker than the starting value of approximately 2.5 hPa/h. This peak in ω_{LS} is not seen for the weakest deciles. Furthermore, the separation into percentiles shows that there is hardly any difference in the temporal signal of the vertical velocity for events in the 80th percentile or higher. Apparently, ω_{LS} levels off for the highest precipitation intensities.

The temporal evolution of CAPE is shown in Figure 7b for deciles (solid) and the top 10 percentiles (dashed) of peak precipitation intensity. The lowest deciles hardly show a signal, but for the highest intensities, there is a strong increase in CAPE leading up to a few hours before the height of the event, after which CAPE drops drastically at the time of the peak intensity. This signal increases for increasing precipitation percentiles. It indicates

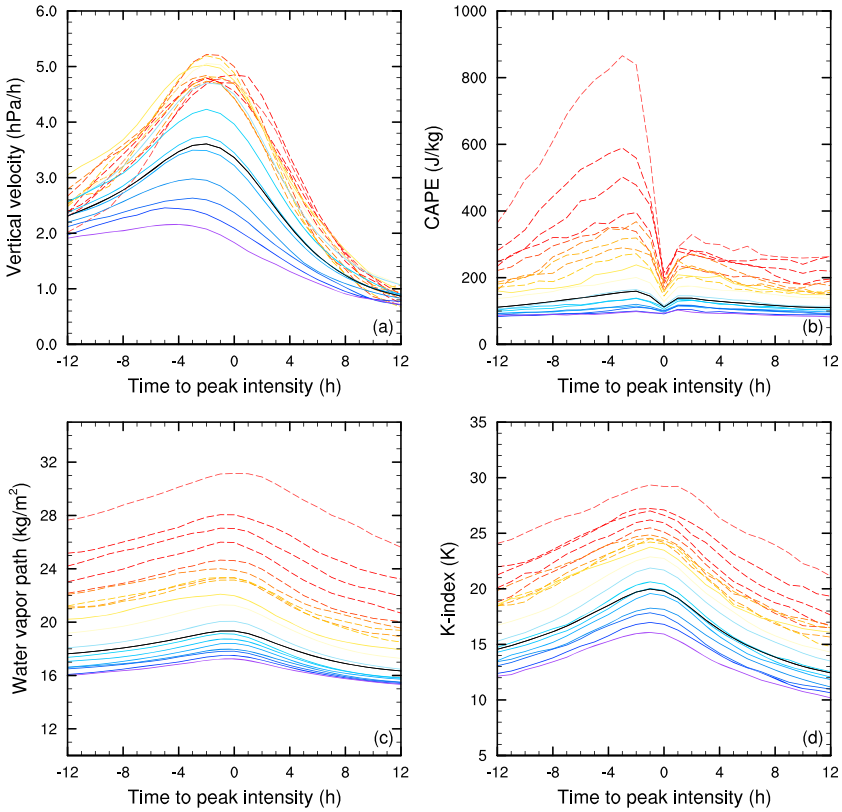

Figure 7. Temporal evolution of (a) large-scale vertical velocity, (b) CAPE, (c) WVP, and (d) *K* index, from 12 h prior to 12 h after the time of the peak intensity of the event. The mean profile is shown in black, while the profiles for increasing precipitation bins are shown from blue (weak precipitation) to red (strong precipitation). The solid lines are decile bins. The highest decile bin has been split up into percentile bins (dashed lines).

a strong destabilization of the atmosphere leading up to the heavy precipitation events, after which CAPE is quickly reduced due to surface cooling and consumption by the event. At the time of the peak intensity, CAPE has reached its minimum value, and CAPE is slightly restored and remains steady at low values.

The temporal evolution of the water vapor path (Figure 7c) shows a modest increase in the water vapor path leading up to the peak intensity, which is most clear for the highest percentiles. As the water vapor is condensed and precipitated out, the atmosphere becomes slightly drier than it was 12 h before the peak intensity. The water vapor path shows hardly any distinction between the lowest deciles, but the spread increases for the highest deciles. The top 10 percentiles show a very strong increase of WVP with increasing intensity.

Figure 7d shows the temporal evolution of the *K* index from 12 h before to 12 h after the maximum precipitation intensity is reached. The spread of increasing *K* index for increasing precipitation intensity deciles is very clear for the top 20% of the peak intensities in this figure. There is also a clear temporal signal, where the *K* index increases up to an hour before the event peaks and decreases afterward to a slightly lower value than it started off with.

4.2. Distributions

The distributions of the atmospheric parameters discussed in this section and the relations between the peak intensity and these parameters are shown in Figure 8. Again, the atmospheric parameters are taken at a 3 h lead with respect to the peak intensity, to keep event-induced effects to a minimum. The data are evaluated for 25 bins of equal sample size of the atmospheric parameter. The black solid line in the top panel of each atmospheric parameter shown in Figure 8 shows the mean relation with the peak intensity. The shaded area indicates the range of the 10th to 90th precipitation percentiles, and the binned 99th percentile is shown by the dashed line. The bottom panels of each parameter shows the distribution of the frequency of occurrence of the parameter values. A good precipitation indicator will show a positive (or negative) relation with peak intensity, with hardly any difference between the different precipitation percentiles and the mean.

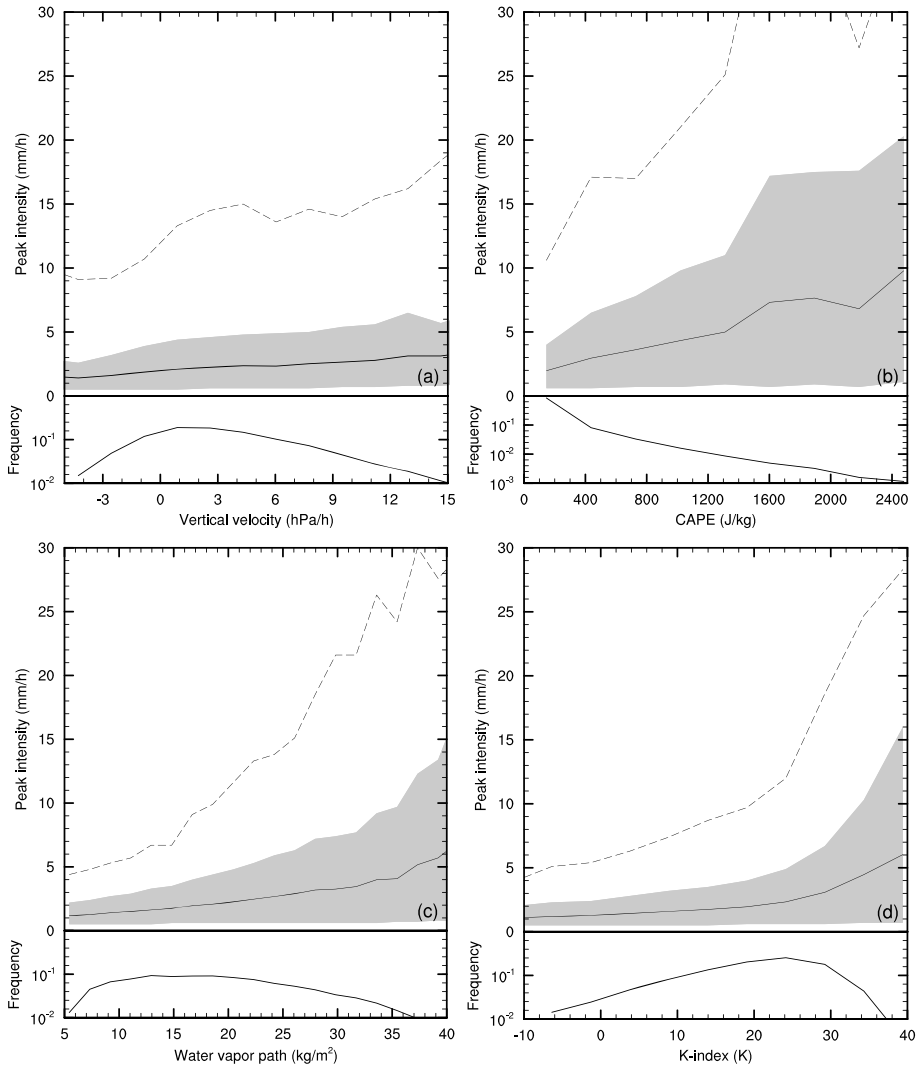

Figure 8. The top pannel of (a) shows the mean vertical velocity 3 h prior to peak intensity versus peak intensity based on 25 of equal sample sizes ω_{LS} bins (solid). The grey shading gives the range from 10th to 90th percentile. The dashed line is 99th percentile. The bottom panel gives the frequency distribution of the vertical velocity. The same is shown for CAPE (b), WVP (c), and the *K* index (d).

The relation between ω_{LS} and the peak intensity is shown in Figure 8a. The bin-averaged peak intensity increases from 1.5 to 3.5 mm/h with increasing large-scale vertical velocity (solid). The 99th percentile increases from approximately 10 to 20 mm/h over the same range of vertical velocity. While most of the data are concentrated around weak ω_{LS} values, there are plenty of data where the vertical velocity exceeds 5 hPa. This means that the leveling off seen in Figure 7a for precipitation percentiles is not due to a physical limit. Instead, it results from the high concentration of data around low ω_{LS} values, in combination with the weak increase in the peak intensity with ω_{LS}. As a consequence, even the heaviest precipitation percentiles will contain a relatively large amount of weak ω_{LS} values, leading to the observed leveling off when we look at the percentile spread in Figure 7a.

The peak intensity shows a stronger increase with CAPE (Figure 8b), from 2 to 10 mm/h. The spread and the 99th percentile also increase with increasing CAPE, indicating that an increase in CAPE leads to a large range of precipitation intensities, both high and low. This may have to do with the fact that CAPE is a potential that does not have to be consumed, increasing the amount of scatter in the relation between CAPE and peak precipitation. However, removing data with a high convective inhibition from the data set has not lead to significant changes in the results (not shown). Most of the data are concentrated around low CAPE values.

Table 3. Maximum Cross Correlations With the Peak Intensity and the Time at Which the Maximum Cross Correlation Is Reached[a]

Variable	Cross Correlation	Time
Vertical velocity	0.15	0 h
CAPE	0.33	−3 h
WVP	0.30	−1 h
K index	0.24	−2 h
LTS	0.10	−1 h
LLM	0.28	−1 h
MLH	0.08	+1 h

[a]The decomposition of the *K* index is shown below the horizontal line.

Figure 8c shows the relation between the water vapor path and peak intensity. The slope of the peak intensity versus the water vapor path increases with increasing water vapor path but does not show the same characteristic critical behavior as can be seen in, e.g., *Peters and Neelin* [2006]. However, this may be due to the fact that the water vapor path does not reach the tropical WVP values at which they observe critical behavior. The peak intensity clearly increases with increasing WVP, from 1 to 6 mm/h in the mean and from 4 to 29 mm/h for the 99th percentile. This, in combination with a reasonably uniform frequency distribution, explains the increase in stratification with increasing deciles of peak precipitation in Figure 7c. The highest precipitation deciles only contain a small range of WVP values, while the lower deciles all contain a large range of WVP values, causing the difference between each weakening decile to decrease. Furthermore, the increasing spread of the peak intensity shows that while low water vapor paths hardly ever result in heavy precipitation, a high water vapor path can lead to a large range of precipitation intensities.

Finally, the relation between the *K* index and the peak intensity is shown in Figure 8d. While for low *K* index values there is hardly any relation with the peak intensity, the peak intensity starts to rapidly increase for *K* index values beyond roughly 20 K. However, the range between the 10th and 90th percentile also increases for the *K* index above 20 K, so that again, a high *K* index does not necessarily have to lead to high precipitation intensities.

4.3. Lag Correlation

So far, we have found clear stratification in the precipitation deciles and percentiles of the atmospheric parameters shown in Figure 7. Furthermore, the peak intensity is positively related to all atmospheric parameters (Figure 8). However, the latter figure also shows a large amount of scatter in these relations, as shown, for instance, by the broad grey shading between the 10th and 90th percentiles. Figure 9 (black lines) shows the lag correlations between ω_{LS} (a), CAPE (b), WVP (c), and the *K* index, and the peak intensity, which enables us to see how the correlation between these parameters and the peak intensity changes in time. The values of the maximum correlations can be found in Table 3.

The CAPE correlation pattern is similar to the temporal evolution seen in Figure 7b. At $t = -3$ h a maximum correlation of 0.33 is reached, after which it drops drastically. As expected from Figure 7b, the correlation reaches its minimum value at $t = 0$ h. The correlation between CAPE and the peak intensity is the highest of all parameters, despite the large amount of scatter seen in Figure 8b. It seems that high CAPE does increase the chance of an extreme event occurring in the next couple of hours, but the relation is not strong enough for CAPE alone to be a good indicator for extreme precipitation. While extreme events are usually preceded by high CAPE values, high CAPE conditions do not necessarily lead to strong precipitation.

The correlation between the water vapor path and the peak intensity has a weaker temporal signal, increasing from 0.26 to 0.30 at $t = -1$ h, after which the correlation gradually decreases to 0.22 at $t = +12$ h. The fact that the correlation is not influenced much by the timing of the event shows that this is more of a climatological correlation; the precipitation intensity is stronger when the atmosphere contains more moisture.

The *K* index correlation with the peak intensity increases from 0.16 at $t = -12$ h to 0.24 at $t = -2$ h, followed by a decrease to 0.14 at $t = +12$ h. Despite the strong increase of peak precipitation with *K* index (Figure 8d), the maximum correlation is weak. Apart from a still significant amount of scatter, this can also be explained by the large range (up to 25 K) where there is hardly any increase in the peak intensity with increasing *K* index.

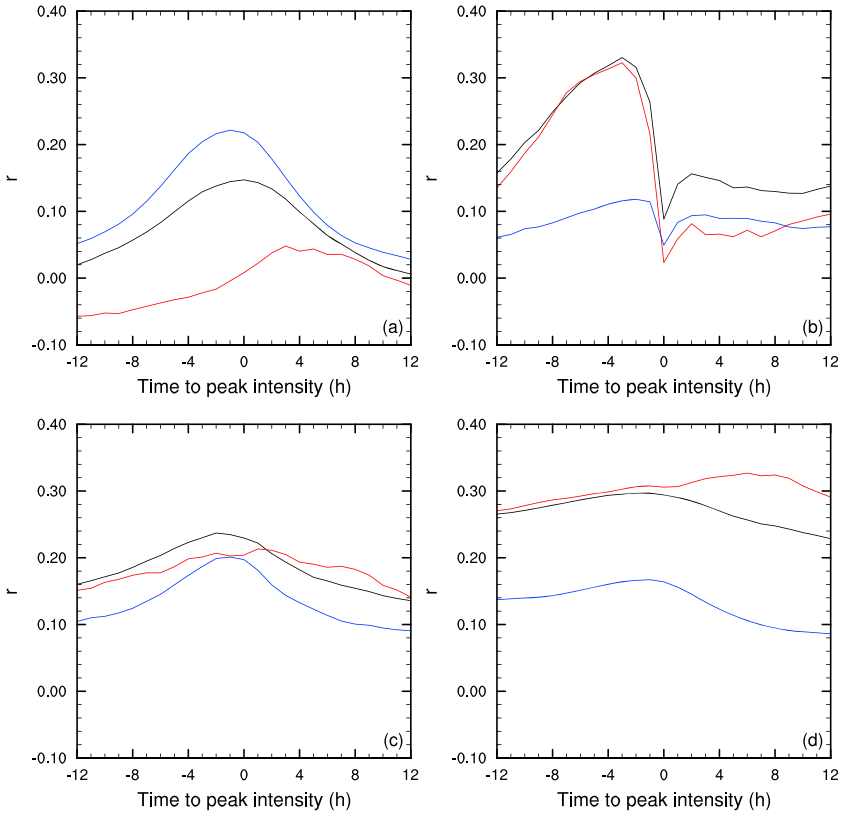

Figure 9. Lag correlations between peak intensity and (a) vertical velocity, (b) CAPE, (c) water vapor path, and (d) the *K* index. The correlation of the whole peak intensity distribution is shown in black. The high intensities (90–100%) are shown in red and the weak to moderate intensities in blue.

Of the three moisture and stability terms that form the *K* index (equation (1)), the correlation with precipitation intensity of the LLM resembles the correlation of the *K* index the most and even exceeds it (Table 3). There is hardly any correlation between precipitation intensity and the MLH or LTS. Apparently, this combination of qualities does not lead to an enhanced correlation with the peak intensity.

In contrast to tropical results [*Dorrestijn et al.*, 2014; *Davies et al.*, 2013], the correlation between the vertical velocity and the peak intensity is almost nonexistent at ±12 h and is nearly symmetrical about the time of the event, at which it peaks at 0.15. This very weak correlation is in line with the leveling off seen in Figure 7a and the weak relation between the vertical velocity and peak intensity seen in Figure 8a. While these figures show that precipitation intensities are more prone to stronger upward velocities, the distinction between moderate (80th percentile) and more extreme precipitation (99th percentile) is weak.

To investigate whether these correlations depend on the intensity range, Figure 9 also shows the correlations for lower intensities (decile range 0 to 90, blue) and the upper decile range (red). While the correlations of CAPE (b), the water vapor path (c), and the *K* index (d) are mainly determined by the highest peak intensities, the correlation with large-scale vertical velocity (a) is mainly controlled by the lower intensities. This is not an unexpected result, since lower intensities often occur in the presence of fronts. Overall, these results suggest that while large-scale vertical velocity tends to be higher for high peak intensities than low peak intensities, the atmospheric stability becomes a controlling factor for more extreme precipitation to occur.

The correlations depicted in Figure 9 are rather weak and follow similar temporal patterns as in Figure 7. It seems counterintuitive for a correlation to be weak, despite the strong stratification for precipitation deciles. But a strong stratification based on precipitation percentiles does not necessarily mean that this parameter will be a good indicator for precipitation. Figure 8 has already shown that there is a large amount of scatter in these relations, which ultimately leads to the weak correlations seen in Figure 9. Even for CAPE, which has the highest peak correlation, Figure 8c shows that a high CAPE can still lead to a large range of peak

intensities. In order to find an atmospheric indicator for extreme precipitation, it may be necessary to combine the atmospheric parameters discussed here.

5. Summary and Final Remarks

With this study, we present a comprehensive statistical analysis of atmospheric conditions for the precipitating atmosphere and precipitation controlling factors at midlatitudes. To this end, in situ precipitation observations over the Netherlands are used in combination with atmospheric data from a high-resolution reanalysis. To remove double counting, the data have been evaluated in an event-based setting.

To gain a better understanding of what the precipitating atmosphere looks like, we have performed profile and temporal analyses of large-scale atmospheric conditions and forcing. Separation of the data into precipitation deciles was used to reveal the change in atmospheric conditions with increasing event intensity. These analyses have shown that heavy precipitation events tend to occur under warmer, moister conditions than weaker events and have a stronger temporal signal.

The large-scale vertical velocity is positive, which is associated with large-scale convergence, and nearly doubles for strong peak intensities with respect to the weakest precipitation decile. The temporal signal also increases for more extreme peak intensities. Driven by vertical advection, the dynamical temperature and moisture tendencies are strongest for the heaviest peak intensities and show cooling and moistening prior to the event. This is largely compensated by the condensation and condensational heating resulting in a precipitation response. The total tendencies, temperature in particular, are much weaker than the separate dynamical (large-scale) and physical (convection) components, suggesting near-convective quasi-equilibrium.

Based on the profile analysis, we have evaluated four atmospheric parameters as potential precipitation indicators at midlatitudes: the large-scale vertical velocity, CAPE, the water vapor path, and the *K* index. The temporal signal tends to increase with increasing precipitation deciles, indicating that these atmospheric parameters are more strongly influenced by the event than weaker events. Furthermore, the stratification of the atmospheric parameters increases for increasing deciles of peak intensity, apart from the vertical velocity, which shows a leveling off for the upper 20% of peak intensities. Overall, the strongest events are prone to stronger convergence and take place under moister, more unstable conditions than weaker events.

However, this does not necessarily mean that, for example, a very unstable atmosphere will always lead to heavy precipitation. In fact, the relations between the peak intensity and all four atmospheric parameters contain a large amount of scatter. The leveling off seen for high precipitation percentiles of ω_{LS} is not caused by a physical process but is induced statistically by the weak increase of peak intensity with vertical velocity and the large spread of the vertical velocity. Because of the large spread, the mean vertical velocity does not increase much with increasing intensity deciles, even though individual values of omega can be much higher. This also leads to a very weak correlation between the large-scale vertical velocity and peak intensity. The other parameters show a stronger increase and also contain large amounts of scatter, again leading to weak correlations. With 0.33, CAPE at −3 h has the highest correlation with the peak precipitation intensity. A decomposition into weak to moderate (<4.7 mm/h) and heavy (>4.7 mm/h) peak intensities has shown that the correlation between peak intensity and CAPE is mainly determined by heavy intensities, while the opposite is true for the vertical velocity.

Interestingly, CAPE and the vertical velocity show large variations in time, whereas atmospheric moisture hardly shows a temporal signal. The *K* index, which is based on both absolute and relative moisture, as well as the vertical temperature gradient, displays an in-between behavior. This suggests that moisture is a background forcing; precipitation tends to be more extreme with higher moisture contents but at the same time does not link very well with the timing of the event. On the other hand, CAPE and the vertical velocity do appear to be linked to the timing of the event. The high variations in CAPE also show that using CAPE from proximity data such as radio sondes has its limitations, possibly explaining the different results reported on the relation between CAPE and precipitation extremes [*Dyson et al.*, 2014; *Barkidija and Fuchs*, 2013].

In summary, we presented an analysis of the relation between atmospheric conditions and large-scale forcing related to precipitation evens of different magnitudes, with an emphasis on the most extreme cases. This research has shown that overall, the strongest precipitation events take place under warmer, moister conditions than weak events, enduring stronger large-scale convergence. The temporal signal of these attributes with respect to the time of the peak intensity increases with increasing peak intensity deciles as well. These

results do not translate to one single indicator for precipitation, unlike the tropics, where strong relations are found between convection and convective precipitation, and the vertical velocity [*Dorrestijn et al.*, 2014; *Davies et al.*, 2013]. Apparently, while high deciles of peak intensity do show a preference for high moisture, instability, and large-scale convergence, none of these conditions are reliable indicators for high precipitation amounts.

Acknowledgments
This study was funded by Knowledge for Climate theme 6. The automated weather station data used in this study can be obtained from www.knmi.nl/uurgegevens. For the RACMO data and the radiosondes used to validate CAPE, contact Geert Lenderink (geert.lenderink@knmi.nl).

References

Allen, J. T., and D. J. Karoly (2014), A climatology of Australian severe thunderstorm environments 1979–2011: Inter-annual variability and ENSO influence, *Int. J. Climatol.*, *34*(1), 81–97, doi:10.1002/joc.3667.

Barkidija, S., and Ž. Fuchs (2013), Precipitation correlation between convective available potential energy, convective inhibition and saturation fraction in middle latitudes, *Atmos. Res.*, *124*, 170–180, doi:10.1016/j.atmosres.2012.12.010.

Berg, P., C. Moseley, and J. O. Haerter (2013), Strong increase in convective precipitation in response to higher temperatures, *Nat. Geosci.*, *6*(3), 181–185.

Blenkinsop, S., S. C. Chan, E. J. Kendon, N. M. Roberts, and H. J. Fowler (2015), Temperature influences on intense UK hourly precipitation and dependency on large-scale circulation, *Environ. Res. Lett.*, *10*(5), 54021.

Bretherton, C. S., and M. E. Peters (2004), Relationships between water vapor path and precipitation over the tropical oceans, *J. Clim.*, *17*, 1517–1528.

Catto, J. L., and S. Pfahl (2013), The importance of fronts for extreme precipitation, *J. Geophys. Res. Atmos.*, *118*(19), 10,791–10,801, doi:10.1002/jgrd.50852.

Charba, J. P. (1977), *Operational System for Predicting Thunderstorms Two to Six Hours in Advance*, National Weather Service, NOAA, Boulder, Colo.

Craven, J. P., and H. E. Brooks (2004), Baseline climatology of sounding derived parameters associated with deep, moist convection, *Nat. Weather Dig.*, *28*, 13–24.

Davies, L., C. Jakob, P. May, V. V. Kumar, and S. Xie (2013), Relationships between the large-scale atmosphere and the small-scale convective state for Darwin, Australia, *J. Geophys. Res. Atmos.*, *118*, 11,534–11,545, doi:10.1002/jgrd.50645.

Dee, D. P., et al. (2011), The ERA-Interim reanalysis: Configuration and performance of the data assimilation system, *Q. J. R. Meteorol. Soc.*, *137*(656), 553–597, doi:10.1002/qj.828.

Dorrestijn, J., D. T. Crommelin, A. P. Siebesma, H. J. J. Jonker, and C. Jakob (2014), Stochastic parameterization of convective area fractions with a multicloud model inferred from observational data, *J. Atmos. Sci.*, *72*(2), 854–869, doi:10.1175/JAS-D-14-0110.1.

Doswell, C. A., and L. F. Bosart (2001), Extratropical synoptic-scale processes and severe convection, *Meteorol. Monogr.*, *28*(50), 27–70, doi:10.1175/0065-9401-28.50.27.

Doswell, C. A., H. E. Brooks, and R. A. Maddox (1996), Flash flood forecasting: An ingredients-based methodology, *Weather Forecasting*, *11*, 560–581, doi:10.1175/1520-0434(1996)011<0560:FFFAIB>2.0.CO;2.

Ducrocq, V., et al. (2013), HyMeX-SOP1: The field campaign dedicated to heavy precipitation and flash flooding in the northwestern Mediterranean, *Bull. Am. Meteorol. Soc.*, *95*, 1083–1100, doi:10.1175/BAMS-D-12-00244.1.

Dyson, L. L., J. van Heerden, and P. D. Sumner (2014), A baseline climatology of sounding-derived parameters associated with heavy rainfall over Gauteng, South Africa, *Int. J. Climatol.*, *127*, 114–127, doi:10.1002/joc.3967.

Emori, S., and S. J. Brown (2005), Dynamic and thermodynamic changes in mean and extreme precipitation under changed climate, *Geophys. Res. Lett.*, *32*, L17706, doi:10.1029/2005GL023272.

Gaál, L., P. Molnar, and J. Szolgay (2014), Selection of intense rainfall events based on intensity thresholds and lightning data in Switzerland, *Hydrol. Earth Syst. Sci.*, *18*(5), 1561–1573, doi:10.5194/hess-18-1561-2014.

Hand, W. H., N. I. Fox, and C. G. Collier (2004), A study of twentieth-century extreme rainfall events in the United Kingdom with implications for forecasting, *Meteorol. Appl.*, *11*(1), 15–31, doi:10.1017/S1350482703001117.

Houze, R. A. (2004), Mesoscale convective systems, *Rev. Geophys.*, *42*, RG4003, doi:10.1029/2004RG000150.

IPCC (2014), *Climate Change 2013: The Physical Science Basis—Working Group I Contribution to the Fifth Assessment Report of the Intergovernmental Panel on Climate Change*, Cambridge Univ. Press, Cambridge, U. K., and New York.

KNMI (2014), Uurgegevens van het weer in Nederland, Royal Netherlands Meteorological Society, De Bilt, Netherlands. [Online; accessed 13-November-2014.]

Lenderink, G., and J. Attema (2015), A simple scaling approach to produce climate scenarios of local precipitation extremes for the Netherlands, *Environ. Res. Lett.*, *10*(8), 85001, doi:10.1088/1748-9326/10/8/085001.

Lenderink, G., and E. V. Meijgaard (2008), Increase in hourly precipitation extremes beyond expectations from temperature changes, *Nat. Geosci.*, *1*(8), 511–514.

Lenderink, G., and E. van Meijgaard (2010), Linking increases in hourly precipitation extremes to atmospheric temperature and moisture changes, *Environ. Res. Lett.*, *5*, 25208.

Lepore, C., D. Veneziano, and A. Molini (2015), Temperature and cape dependence of rainfall extremes in the eastern United States, *Geophys. Res. Lett.*, *42*, 74–83, doi:10.1002/2014GL062247.

Loriaux, J. M., G. Lenderink, S. R. de Roode, and A. P. Siebesma (2013), Understanding extreme convective precipitation scaling using observations and an entraining plume model, *J. Atmos. Sci.*, *70*(11), 3641–3655, doi:10.1175/JAS-D-12-0317.1.

Min, S.-K., X. Zhang, F. W. Zwiers, and G. C. Hegerl (2011), Human contribution to more-intense precipitation extremes, *Nature*, *470*(7334), 378–381.

Molnar, P., S. Fatichi, L. Gaál, J. Szolgay, and P. Burlando (2015), Storm type effects on super Clausius-Clapeyron scaling of intense rainstorm properties with air temperature, *Hydrol. Earth Syst. Sci.*, *19*(4), 1753–1766, doi:10.5194/hess-19-1753-2015.

O'Gorman, P. A. (2015), Precipitation extremes under climate change, *Curr. Clim. Chang. Rep.*, *1*(2), 49–59.

O'Gorman, P. A., and T. Schneider (2009), The physical basis for increases in precipitation extremes in simulations of 21st-century climate change, *Proc. Natl. Acad. Sci. U.S.A.*, *106*, 14,773–14,777.

Pall, P., T. Aina, D. A. Stone, P. A. Stott, T. Nozawa, A. G. J. Hilberts, D. Lohmann, and M. R. Allen (2011), Anthropogenic greenhouse gas contribution to flood risk in England and Wales in autumn 2000, *Nature*, *470*(7334), 382–385.

Peters, O., and J. D. Neelin (2006), Critical phenomena in atmospheric precipitation, *Nat. Phys.*, *2*, 393–396.

Pfahl, S., and H. Wernli (2012), Quantifying the relevance of cyclones for precipitation extremes, *J. Clim.*, *25*(19), 6770–6780.

Van Meijgaard, E., L. H. Van Ulft, W. J. Van de Berg, F. C. Bosveld, B. J. J. M. Van den Hurk, G. Lenderink, and A. P. Siebesma (2008), *The KNMI Regional Atmospheric Climate Model RACMO Version 2.1*, Koninklijk Nederlands Meteorologisch Instituut.

Westra, S., H. J. Fowler, J. P. Evans, L. V. Alexander, P. Berg, F. Johnson, E. J. Kendon, G. Lenderink, and N. M. Roberts (2014), Future changes to the intensity and frequency of short-duration extreme rainfall, *Rev. Geophys.*, *52*, 522–555, doi:10.1002/2014RG000464.

Zhang, G. J. (2002), Convective quasi-equilibrium in midlatitude continental environment and its effect on convective parameterization, *J. Geophys. Res.*, *107*(D14), 4220, doi:10.1029/2001JD001005.

Zhang, G. J. (2003), Convective quasi-equilibrium in the tropical western Pacific: Comparison with midlatitude continental environment, *J. Geophys. Res.*, *108*(D19), 4592, doi:10.1029/2003JD003520.